Enhanced Electron Injection into Inverted Polymer Light-Emitting Diodes by Combined Solution-Processed Zinc Oxide/Polyethylenimine Interlayers

ARTICLE *in* ADVANCED MATERIALS · MAY 2014

Impact Factor: 17.49 · DOI: 10.1002/adma.201304666 · Source: PubMed

5 AUTHORS, INCLUDING:

Stefan Höfle
Karlsruhe Institute of Technology
12 PUBLICATIONS **88** CITATIONS
SEE PROFILE

Uli Lemmer
Karlsruhe Institute of Technology
421 PUBLICATIONS **7,248** CITATIONS
SEE PROFILE

Alexander Colsmann
Karlsruhe Institute of Technology
78 PUBLICATIONS **976** CITATIONS
SEE PROFILE

Enhanced Electron Injection into Inverted Polymer Light-Emitting Diodes by Combined Solution-Processed Zinc Oxide/Polyethylenimine Interlayers

Stefan Höfle, Alexander Schienle, Michael Bruns, Uli Lemmer, and Alexander Colsmann**

Due to their planar nature and their mechanical flexibility, organic light emitting diodes (OLEDs) open pathway to many new applications in display technology, signage and general lighting. While state-of-the-art OLEDs are mostly fabricated by thermal evaporation in vacuum, solution processing (printing and coating) is widely discussed for future cost reduction in OLED fabrication. So far, vacuum processed devices outperform their solution processed counterparts not least because thermal evaporation allows for stacking an arbitrary number of functional layers while solution deposition is ruled by solvent limitations. In vacuum processed OLEDs, charge carrier injection can be facilitated by utilizing electrically doped organic semiconductor layers.[1–3] Alternatively, high-work function metal oxides such as molybdenum oxide (MoO_3),[4,5] tungsten oxide (WO_3)[6,7] or vanadium pentoxide (V_2O_5)[8,9] can be used for the injection of holes. Recently, we have demonstrated that MoO_3 or WO_3 hole injection layers for OLEDs can also be applied via a facile precursor route from molybdenum(V)ethoxide, tungsten(V)ethoxide or tungsten(VI)ethoxide, respectively.[10,11]

On the other hand, electron injection into the lowest unoccupied molecular orbital (LUMO) level of light emitting or adjacent electron transport materials is much more challenging since it requires low-work function and hence reactive electrodes, interface modifiers or buffer layers such as calcium, lithium fluoride/aluminium or lithium-doped bathophenanthroline.[12–14] Due to their reactivity, however, those materials are mostly incompatible with solution processing. In the closely related research field of organic photovoltaics, metal oxides such as titanium oxide or zinc oxide have been investigated for efficient electron extraction. These metal oxides can be applied via precursor routes, partly at moderate temperatures.[15–20] These processes have been partly transferred to OLED applications.[21–24] But because of the still high work function of ZnO ($\Phi_a \approx 4.1$ eV), the injection barrier between ZnO and the adjacent organic layer only allows the fabrication of moderately efficient OLEDs. An interesting alternative to modify the work function of the electrode towards enhanced electron injection are strong dipole moments of self-assembled monolayers (SAMs) or physisorbed interlayers.[25–27] The strength of such dipoles depends very much on the physical and electrical interaction with the surface of the subjacent layer. Often, interlayers exhibit superior bonding abilities with metal oxides such as indium tin oxide (ITO).[28,29] Interlayers can be established from either low-molecular weight materials or polymers. Recently, polymeric dipole layers from polyethyleneimine (PEI),[30,31] polyethylenimine ethoxylated (PEIE)[31] and poly [(9,9-bis(3-(N,N-dimethylamino)propyl)-2,7-fluorene)-alt-2,7-(9,9–dioctylfluorene)][32] were investigated. In particular, PEI and PEIE are known to exhibit a high dipole moment on many different surfaces like ZnO, indium tin oxide (ITO), poly(3,4-ethylenedioxythiophene):poly(styrenesulfonate) (PEDOT:PSS), gold, silver and aluminum.[31] Employing a polyelectrolyte for improved electron injection into inverted OLEDs enabled current efficiencies of up to 3.5 cd A^{-1}.[33,34]

In this work we investigate an efficient and air-stable, two-step electron injection from a high-work function ITO cathode into inverted fluorescent OLEDs through PEI physisorbed interlayers with high dipole moments on ZnO buffer layers. Additional replacement of the aluminum top-anode by the conductive polymer PEDOT:PSS enables full solution processing of transparent polymer OLEDs.

Inverted OLEDs: In order to efficiently inject electrons from the high-work function ITO into the LUMO of the light emitting polymer Super Yellow ($E_{LUMO} \approx -3.0$ eV) in an inverted OLED, we utilized the device architecture illustrated in **Figure 1**a. Figure 1b depicts the proposed energy levels of the functional layers throughout the fluorescent OLED. First, we spin cast the $Zn(acac)_2$ precursor from ethanol solution on indium tin oxide (ITO) substrates under ambient conditions. The precursor was subsequently converted to ZnO in a gentle

S. Höfle, A. Schienle, Dr. A. Colsmann
Light Technology Institute
Karlsruhe Institute of Technology (KIT)
Engesserstrasse 13, 76131 Karlsruhe, Germany
E-mail: stefan.hoefle@kit.edu;
alexander.colsmann@kit.edu
Dr. M. Bruns
Institute for Applied Materials and Karlsruhe
Nano Micro Facility (KNMF)
Karlsruhe Institute of Technology (KIT)
Hermann-von-Helmholtz-Platz 1
76344 Eggenstein-Leopoldshafen, Germany
Prof. Dr. U. Lemmer
Light Technology Institute
Karlsruhe Institute of Technology (KIT)
Engesserstrasse 13, 76131 Karlsruhe, Germany
Prof. Dr. U. Lemmer
Institute for Microstructure Technology
Karlsruhe Institute of Technology (KIT)
Hermann-von-Helmholtz-Platz 1
76344 Eggenstein-Leopoldshafen, Germany

DOI: 10.1002/adma.201304666

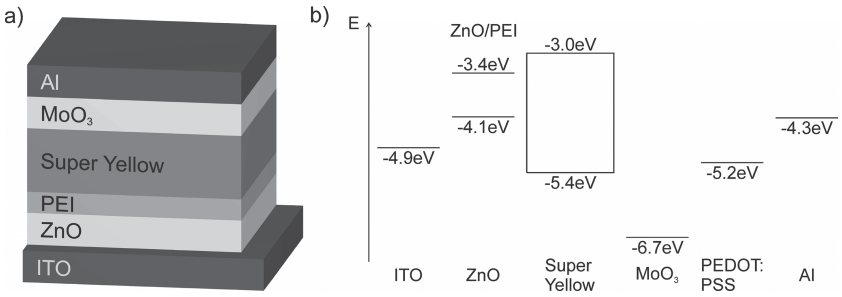

Figure 1. (a) Inverted fluorescent OLED device architecture comprising the light emitting Super Yellow and transparent bottom cathodes from ITO, ZnO and monolayers of PEI. A MoO_3/Al anode completes the opaque device. (b) Proposed energy levels of the OLED.

annealing process (T = 120 °C). Then, PEI was applied from 2-ethoxymethanol solution. For reference and comparison, we investigated OLEDs with (i) plain ITO cathodes, (ii) ITO cathodes with ZnO buffer layers and (iii) ITO cathodes with PEI interface modification. Due to the high work function $\Phi_a \approx$ 4.9 eV of ITO (see XPS measurements in **Figure 2**) and consequently the very high injection barrier for electrons of about 1.9 eV to the Super Yellow LUMO ($E_{LUMO} \approx -3.0$ eV), devices with plain ITO cathodes did not show any electroluminescence at all and therefore were discarded. According to the XPS measurements in Figure 2, the work function of the cathode was reduced to 4.1 eV by applying a ZnO buffer layer. This application of ZnO enabled reasonable electron injection and device onset voltages of 3.2 eV. For ITO/PEI cathodes omitting any ZnO buffer layers, we found a very favorable cathode work function $\Phi_a \approx$ 3.3 eV. Unfortunately, the respective OLED performance was very poor and irreproducible, probably due to exciton quenching in the vicinity of the ITO electrode. However, by combining the ZnO buffer and spacer layer with the PEI interface modifier, the OLED performance and onset voltage was drastically improved: the work function of the ITO/ZnO/PEI electrode $\Phi_a \approx$ 3.4 eV enables an onset voltage of 2.1 V, matching the band-gap energy of Super Yellow and implying an almost barrier free electron injection into the emission layer. The current density-voltage-luminance (JVL) characteristics of the OLEDs are depicted in **Figure 3**a.

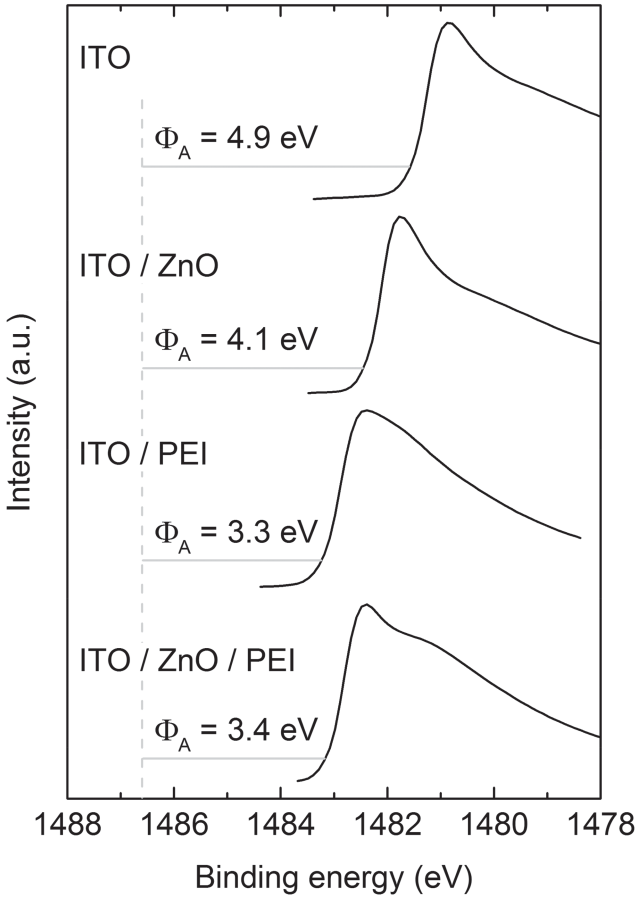

Figure 2. Work functions of ITO, ITO/ZnO, ITO/PEI and ITO/ZnO/PEI electrodes as determined by XPS measurements. The work functions were calculated from the X-ray photon energy (AlKα = 1486.6 eV) and the low kinetic energy spectrum cut-off of the respective sample; the energy scale was referenced to the sample's Fermi level = 0 eV .

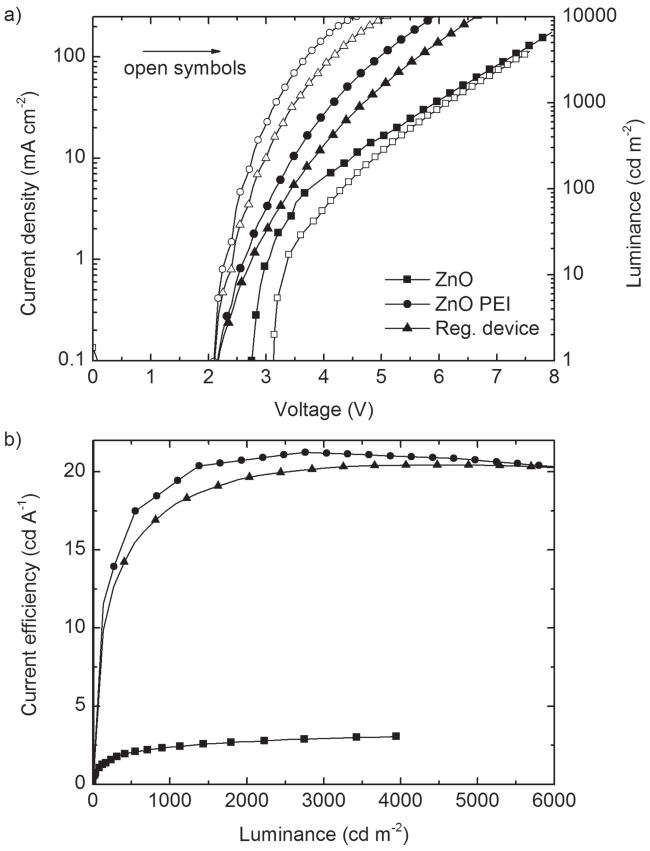

Figure 3. (a) JVL curves of solution processed inverted OLEDs comprising ITO/ZnO or ITO/ZnO/PEI cathodes. The ZnO/PEI electron injection layers enable enhanced device currents and consequently higher luminance. (b) The device current efficiency versus luminance of OLEDs with ITO/ZnO/PEI cathodes. Devices with ITO/ZnO/PEI cathodes clearly outperform their ITO/ZnO counterparts and match the performance of devices with regular architecture.

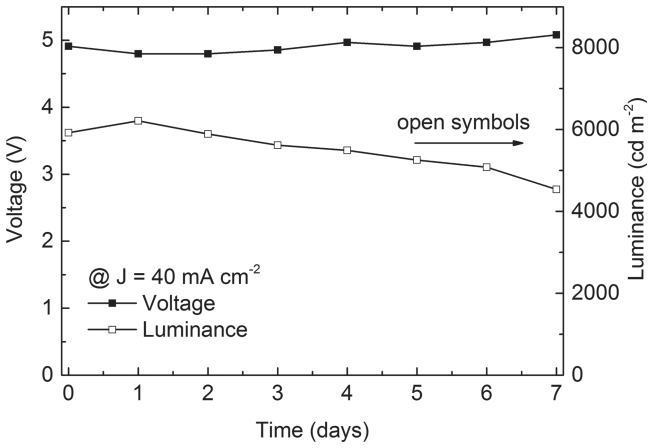

Figure 4. Voltage and luminance of ambiently stored inverted OLEDs comprising ITO/ZnO/PEI cathodes versus time at a device current density of $J = 40$ mA cm^{-2}. The driving voltage is about constant for one week. The device luminance shows only minor decay.

For devices with ITO/ZnO cathode, current efficiencies of ~2 cd A^{-1} were achieved (Figure 3b). Due to the reduced injection barrier for electrons, the device current densities increase dramatically upon utilizing an ITO/ZnO/PEI cathode. Comprising a combination of ZnO and PEI, the OLEDs clearly outperform all reference devices and the efficiencies improve to ~22 cd A^{-1} over a much wider luminance range. In essence, the performance of these inverted OLEDs comprising ITO/ZnO/PEI cathodes matches the performance of (fluorescent) Super Yellow devices built in regular ITO/MoO_3/Super Yellow/LiF/Al device architecture that is plotted in Figure 3 for comparison.

Device Stability: The inverted OLED device architecture comprising ITO/ZnO/PEI cathodes for enhanced electron injection renders the use of reactive cathodes such as calcium or LiF/Al obsolete and hence is the basis for more stable devices. In order to investigate the OLED stability in air, we compared the inverted OLEDs with devices in standard architecture comprising state-of-the-art ITO/PEDOT:PSS anodes and LiF/Al cathodes. After fabrication and initial inert characterization, we investigated the shelf-lifetime of the non-encapsulated devices under ambient conditions with repetitive testing over several days. Without air contamination at a device current density $J = 40$ mA cm^{-2}, the luminance is somewhat higher for the reference device with regular architecture ($L_{reg} = 8600$ cd m^{-2}) than for the inverted device ($L_{inv} = 5900$ cd m^{-2}). After only a couple of hours in air, however, the reference showed strong degradation, i.e. dark spots in the active area. After about one day, it was impossible to maintain the 40 mA cm^{-2} device current. Even at lower device currents, the number and size of these dark spots steadily increased until complete device failure after seven days (data not shown here). Similar device degradation has already been observed for organic solar cells with LiF/Al cathodes.[35] Over seven days, no dark spots were observed at all in the inverted devices despite constant exposure to ambient conditions. **Figure 4** shows the device voltage and luminance at a constant device current density of 40 mA cm^{-2} versus time. The inverted devices exhibited only minor luminance decay from 4900 cd m^{-2} to 4550 cd m^{-2}. The device driving voltage to obtain the desired current density of 40 mA cm^{-2} also remained about constant over the time of investigation.

Due to this very good air stability, we consider the presented inverted device architecture very promising for future OLEDs. It may also enable ambient fabrication of solution processable devices though an inert encapsulation may be mandatory for long-time stability.

Transparent OLEDs: The inverted device architecture is not only more stable in air but also enables transparent OLEDs by replacing the opaque aluminum with a highly conductive, high-work function PEDOT:PSS electrode. The respective JVL curves and current efficiencies are depicted in **Figure 5**. In comparison to the opaque device, the luminance of the transparent OLED is decreased. Subsequently, this leads to a current efficiency reduction by about a factor of eight, i.e. an effective reduction by a factor of four since roughly half the light is lost through the rear electrode. This loss in luminance and current efficiency mainly can be attributed to quenching of the light emission by the PEDOT:PSS layer as it was demonstrated by van Dijken for poly-(p-phenylenevinylene) emitters.[36] Furthermore, the slope of the linear regime of the *J–V* curve indicates a dominant series resistance $R_s = 114\ \Omega cm^2$ that we attribute to the lower conductivity of PEDOT:PSS as compared to the metal electrode in opaque devices ($R_s = 2.3\ \Omega cm^2$). Despite these losses, the device luminance is still high enough for display applications.

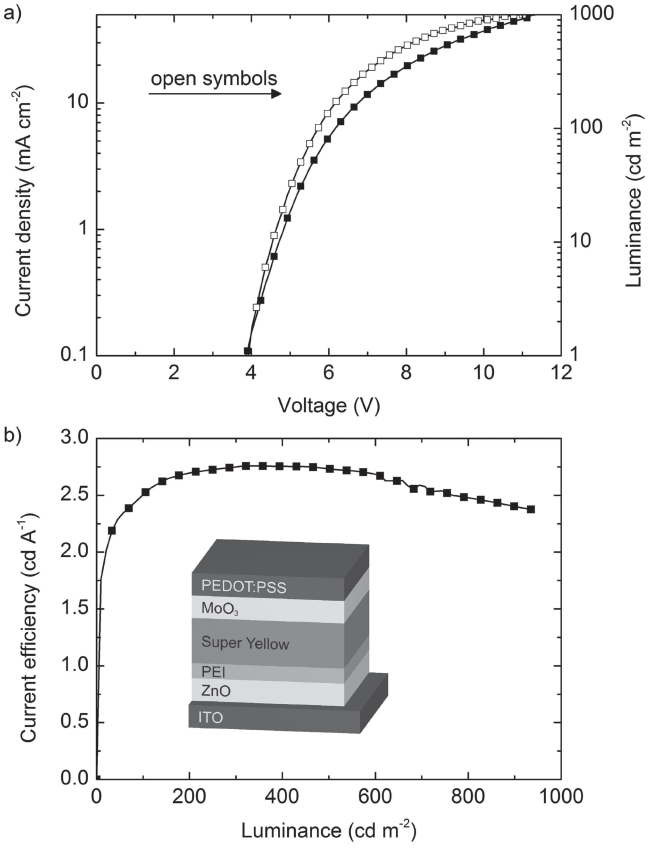

Figure 5. (a) JVL characteristics of a typical transparent OLED. The small slope of the *J–V* curve at high voltages indicates a dominant series resistance due to the limited conductivity of the PEDOT:PSS counter electrode. (b) Device current efficiency versus luminance.

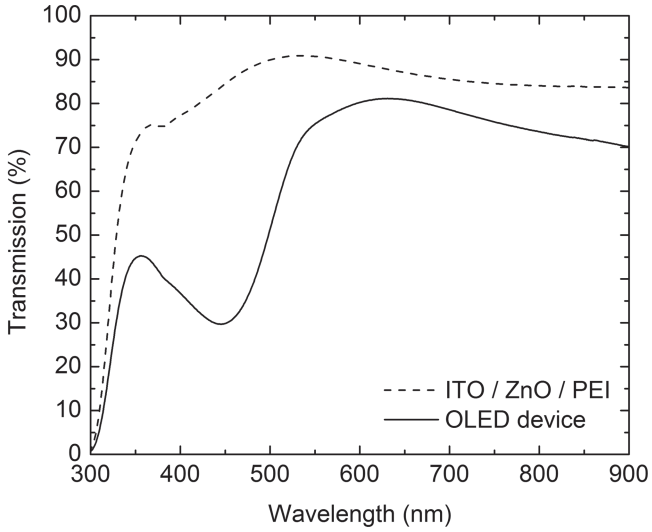

Figure 6. Transmission spectrum of the ITO/ZnO/PEI cathode and of the entire transparent OLED.

In the transparent OLED, the device driving voltage increases, i.e. the *J–V* curve shifts to higher voltages. The high series resistance of the PEDOT:PSS top electrode is further reflected in the onset voltage increase to 3.9 V. The onset current density J_{ON} = 0.04 mA/cm^2 in the opaque device slightly increases to J_{ON} = 0.11 mA/cm^2 in the transparent OLED which we again attribute to light quenching at the PEDOT:PSS electrode and an increased injection barrier due to wetting agents reducing the MoO_3/PEDOT:PSS electrode work function, as we have demonstrated for semi-transparent organic solar cells before.[37] We note that we observed the same effect of the PEDOT:PSS electrode on the optoelectronic properties and the onset voltage of regular OLEDs as described in the Supplementary Information. The transmittance of the OLEDs in **Figure 6** is mainly ruled by the Super Yellow emission layer. Subtracting the specific Super Yellow absorption from the total device absorption leads to a transmission exceeding 70% over the entire visible spectrum, enabling excellent transparency upon future replacement of Super Yellow by wide-gap emitter polymers with suitable molecular doping for color control if necessary.

Experimental Section

According to the device architecture depicted in Figure 1a, all OLEDs were fabricated on indium tin oxide (ITO) coated glass substrates ($R_{\square} \approx$ 13 Ω/□) that had been structured in a hydrochloric acid. The substrates were cleaned with acetone and isopropanol in an ultrasonic bath (15 min). Afterwards the substrates were exposed to an oxygen plasma (2 min) in order to remove organic residues and to polarize the ITO surface for better zinc oxide (ZnO) precursor adhesion.

The deposition of the ZnO layer was based on the process described by Bruyn et al.[17] Accordingly, zinc acetylacetonate hydrate ($Zn(acac)_2$, Sigma-Aldrich) was dissolved in ethanol (20 g L^{-1}) and stirred (24 h, T = 50 °C). Afterwards we filtered the solution with a polytetrafluoroethylene (PTFE) filter (0.2 µm) to remove precursor aggregates. The $Zn(acac)_2$ solution was spin cast (2000 rpm, 45 s) and subsequently annealed (30 s, 120 °C) in ambient atmosphere. Then PEI was spin cast from a 2-methoxyethanol solution (0.4 wt.%, 5000 rpm, 50 s) according to the process suggested by Zhou et al.[31] Afterwards, the samples were annealed in ambient atmosphere (10 minutes, 100 °C) and rinsed with water in order to remove any PEI surplus. A Super Yellow emission layer (Merck) was spin cast from toluene solution (4 g L^{-1}, 1000 rpm, 45 s). Finally, a MoO_3/aluminum (10 nm/200 nm) counter electrode was thermally evaporated in high vacuum (10^{-6} mbar). The intersection of the top anode and the ITO cathode defined an active device area of 5 × 5 mm^2. For the transparent device, the aluminum electrode was replaced by spin cast PEDOT:PSS (Heraeus PH1000, 1000 rpm, 120 s) mixed with dimethyl sulfoxide (DMSO, 5 vol%) and surfactants that increase the conductivity and wettability, respectively.

The OLED current density–voltage (*J–V*) characteristics were recorded with a source measure unit (Keithley 238). The device luminance was calculated from the emission spectrum in forward direction. The spectrometer had been calibrated with a secondary standard calibration halogen lamp (Philips FEL-1000 W). Current efficiencies (cd A^{-1}) and power efficiencies (lm W^{-1}) were calculated from the electrical and optical properties. For this calculation we assumed Lambertian light distribution.

The work functions were determined by X-ray photoelectron spectroscopy (XPS, Thermo Fisher Scientific K-Alpha) using a bias sample holder to measure both the low kinetic energy spectrum cut-off and the Fermi level at a –30 V bias voltage.

Supporting Information

Supporting Information is available from the Wiley Online Library or from the author.

Acknowledgements

This work was supported by the Federal Ministry of Education and Research (Project PrintOLED, grant no. 13N12281). The authors thank the DFG Center for Functional Nanostructures (CFN) for support. S.H. acknowledges support by the Karlsruhe School of Optics & Photonics (KSOP).

Received: September 17, 2013
Revised: February 17, 2014
Published online: March 31, 2014

[1] J. Blochwitz, M. Pfeiffer, T. Fritz, K. Leo, *Appl. Phys. Lett.* **1998**, *73*, 729.
[2] X. Zhou, M. Pfeiffer, J. Blochwitz, A. Werner, A. Nollau, T. Fritz, K. Leo, *Appl. Phys. Lett.* **2001**, *78*, 410.
[3] B. Maennig, M. Pfeiffer, A. Nollau, X. Zhou, K. Leo, *Phys. Rev. B* **2001**, *64*, 195208.
[4] H. You, Y. Dai, Z. Zhang, D. Ma, *J. Appl. Phys.* **2007**, *101*, 026105.
[5] T. Matsushima, G.-H. Jin, H. Murata, *J. Appl. Phys.* **2008**, *104*, 054501.
[6] J. Meyer, S. Hamwi, T. Bülow, H.-H. Johannes, T. Riedl, W. Kowalsky, *Appl. Phys. Lett.* **2007**, *91*, 113506.
[7] T.-Y. Chu, J.-F. Chen, S.-Y. Chen, C.-J. Chen, C. H. Chen, *Appl. Phys. Lett.* **2006**, *89*, 053503.
[8] J. Wu, J. Hou, Y. Cheng, Z. Xie, L. Wang, *Semiconductor Sci. Technol.* **2007**, *22*, 824.
[9] H. M. Zhang, W. C. H. Choy, *J. Phys. D: Appl. Phys.* **2008**, *41*, 062003.
[10] S. Höfle, H. Do, E. Mankel, M. Pfaff, Z. Zhang, D. Bahro, T. Mayer, W. Jaegermann, D. Gerthsen, C. Feldmann, U. Lemmer, A. Colsmann, *Org. Electron.* **2013**, *14*, 1820.
[11] S. Höfle, M. Bruns, S. Strässle, C. Feldmann, U. Lemmer, A. Colsmann, *Adv. Mater.* **2013**, *25*, 4113.

[12] A. Berntsen, Y. Croonen, C. Liedenbaum, H. Schoo, R.-J. Visser, J. Vleggaar, P. van de Weijer, *Opt. Mater.* **1998**, *9*, 125.
[13] L. S. Hung, C. W. Tang, M. G. Mason, *Appl. Phys. Lett.* **1997**, *70*, 152.
[14] J. Huang, M. Pfeiffer, A. Werner, J. Blochwitz, K. Leo, S. Liu, *Appl. Phys. Lett.* **2002**, *80*, 139.
[15] S. K. Hau, H.-L. Yip, O. Acton, N. S. Baek, H. Maa, A. K.-Y. Jen, *J. Mater. Chem.* **2008**, *18*, 5113.
[16] T. Kuwabara, T. Nakayama, K. Uozumi, T. Yamaguchi, K. Takahashi, *Solar Energy Mat. Solar Cells* **2008**, *92*, 1476.
[17] P. de Bruyn, D. J. D. Moet, P. W. M. Blom, *Org. Electron.* **2010**, *11*, 1419.
[18] Y. Sun, J. H. Seo, C. J. Takacs, J. Seifter, A. J. Heeger, *Adv. Mater.* **2011**, *23*, 1679.
[19] M. J. Tan, S. Zhong, J. Li, Z. Chen, W. Chen, *Appl. Mater. Interfaces* **2013**, *11*, 4696.
[20] A. Colsmann, M. Reinhard, T.-H. Kwon, C. Kayser, F. Nickel, J. Czolk, U. Lemmer, N. Clark, J. Jasieniak, A. B. Holmes, D. Jones, *Solar Energy Mater. Solar Cells* **2012**, *98*, 118.
[21] K. Morii, M. Ishida, T. Takashima, T. Shimoda, Q. Wang, M. K. Nazeeruddin, M. Grätzel, *J. Appl. Phys.* **2006**, *89*, 183510.
[22] H. J. Bolink, E. Coronado, D. Repetto, M. Sessolo, *Appl. Phys. Lett.* **2007**, *91*, 223501.
[23] H. J. Bolink, E. Coronado, D. Repetto, M. Sessolo, E. M. Barea, J. Bisquert, G. Garcia-Belmonte, J. Prochazka, L. Kavan, *Adv. Funct. Mater.* **2008**, *18*, 145.
[24] M. Sessolo, H. J. Bolink, *Adv. Mater.* **2011**, *23*, 1829.
[25] S. A. Paniagua, P. J. Hotchkiss, S. C. Jones, S. R. Marder, A. Mudalige, F. S. Marrikar, J. E. Pemberton, N. R. Armstrong, *J. Phys. Chem. C* **2008**, *112*, 7809.
[26] P. J. Hotchkiss, H. Li, P. B. Paramonov, S. A. Paniagua, S. C. Jones, N. R. Armstrong, J.-L. Brédas, S. R. Marder, *Adv. Mater.* **2009**, *21*, 4496.
[27] P. J. Hotchkiss, S. C. Jones, S. A. Paniagua, A. Sharma, B. Kippelen, N. R. Armstrong, S. R. Marder, *Acc. Chem. Res.* **2012**, *45*, 337.
[28] S. Besbes, A. Ltaief, K. Reybier, L. Ponsonnet, N. Jaffrezic, J. Davenas, H. Ben Ouada, *Synt. Met.* **2003**, *138*, 197.
[29] S. Besbes, H. B. Ouada, J. Davenas, L. Ponsonnet, N. Jaffrezic, P. Alcouffe, *Mater. Sci. Eng. C* **2006**, *26*, 505.
[30] J. Chen, C. Shi, Q. Fu, F. Zhao, Y. Hu, Y. Feng, D. Ma, *J. Mater. Chem.* **2012**, *22*, 5164.
[31] Yi. Zhou, C. Fuentes-Hernandez, J. Shim, J. Meyer, A. J. Giordano, H. Li, P. Winget, T. Papadopoulos, H. Cheun, J. Kim, M. Fenoll, A. Dindar, W. Haske, E. Najafabadi, T. M. Khan, H. Sojoudi, S. Barlow, S. Graham, J.-L. Brédas, S. R. Marder, A. Kahn, B. Kippelen, *Science* **2012**, *336*, 327.
[32] Z. He, C. Zhong, S. Su, M. Xu, H. Wu, Y. Cao, *Nat. Photonics* **2012**, *6*, 591.
[33] H. J. Bolink, H. Brine, E. Coronado, M. Sessolo, *ACS Appl. Mater. Interfaces* **2010**, *2*, 2269.
[34] H. Brine, J. F. Sánchez-Royo, H. J. Bolink, *Org. Electron.* **2013**, *14*, 164.
[35] S. K. Hau, H.-L. Yip, N. S. Baek, J. Zou, K. O'Malley, A. K. -Y. Jen, *Appl. Phys. Lett.* **2008**, *92*, 253301.
[36] A. v. Dijken, A. Perro, E. A. Meulenkamp, K. Brunner, *Org. Electron.* **2003**, *4*, 131.
[37] J. Czolk, A. Puetz, D. Kutsarov, M. Reinhard, U. Lemmer, A. Colsmann, *Adv. Energy Mater.* **2013**, *3*, 386.